Aerodynamic State and Loads Estimation Using Bioinspired Distributed Sensing

Sergio A. Araujo-Estrada* and Shane P. Windsor†
University of Bristol, Bristol, England BS8 1TR, United Kingdom

https://doi.org/10.2514/1.C036224

Flying animals exploit highly nonlinear dynamics to achieve efficient and robust flight control. It appears that the distributed flow and force sensor arrays found in flying animals are instrumental in enabling this performance. Using a wind-tunnel wing model instrumented with distributed arrays of strain and pressure sensors, we characterized the relationship between the distributed sensor signals and aerodynamic and load-related variables. Estimation approaches based on nonlinear artificial neural networks (ANNs) and linear partial least squares were tested with different combinations of sensor signals. The ANN estimators were accurate and robust, giving good estimates for all variables, even in the stall region when the distributed array pressure and strain signals became unsteady. The linear estimator performed well for load estimates but was less accurate for aerodynamic variables such as angle of attack and airspeed. Future applications based on distributed sensing could include enhanced flight control systems that directly use measurements of aerodynamic states and loads, allowing for increase maneuverability and improved control of unmanned aerial vehicles with high degrees of freedom such as highly flexible or morphing wings.

Nomenclature

b	=	wing model span, m
C_P	=	pressure coefficient
c	=	wing model mean aerodynamic chord, m
$D, \hat{D}$	=	measured and estimated aerodynamic drag forces, N
$e_{\hat{D}}$	=	aerodynamic drag force estimation error, %
$e_{\hat{L}}$	=	aerodynamic lift force estimation error, %
$e_{\hat{M}}$	=	aerodynamic pitching moment estimation error, %
$e_{\hat{V}}$	=	wind speed estimation error, m/s
$e_{\hat{\alpha}}$	=	angle-of-attack estimation error, deg
$L, \hat{L}$	=	measured and estimated aerodynamic lift forces, N
$M, \hat{M}$	=	measured and estimated aerodynamic pitching moments, N · m
q	=	wing model pitch rate, deg/s
S	=	wing model reference surface, m^2
T	=	normalized strain due to torsion, $mV/(N \cdot m)$
$V, \hat{V}$	=	measured and estimated wind speed, m/s
VB	=	normalized vertical bending moment
$\alpha, \hat{\alpha}$	=	measured and estimated angle of attack, deg
ρ	=	air density, kg/m^3

I. Introduction

CONVENTIONAL flight control systems for autonomous aircraft traditionally use a small number of very precise sensors, which give the control system information about the motion of the aircraft's center of mass. For instance, inertial measurement units are used to measure linear acceleration and angular rates of rotation, whereas a pitot tube is used to measure airspeed. This information is then normally used alongside sensors such as the Global Positioning System to provide the control system with measurements of the aircraft rigid-body motion [1]. This combination of conventional sensor suites and controllers works well when the assumptions of rigid-body motion and linearized flight dynamics and aerodynamics apply but may be limiting when these assumptions are no longer valid: for example, with highly flexible airframes or at high angles of attack. In some cases, the flight dynamics and aerodynamics models may be too simple to capture highly nonlinear dynamics; whereas in other cases, the type, number, and placement of sensors used may not be adequate.

Biological fliers such as birds, bats, and insects all have highly flexible wings and bodies, where numerous joints and aeroelastic deformation mean that the shapes of their wings and the related aerodynamic forces they produce are constantly changing [2]. In addition, they fly in airflows where the magnitude of the gusts can be the same order as their airspeed, meaning that they can experience very large unpredictable changes in angle of attack [3]. Rather than being limited by these departures from rigid-body motion and linear aerodynamics, it appears that biological fliers take advantage of them. For instance, wing flexibility helps reduce the flight costs of locusts [4], flapping motion generates additional lift through leading-edge vortex generation in bats [5], and birds appear to use both spatial [6] and temporal variations [7] in the wind to reduce their flight costs.

One aspect all biological fliers appear to have in common, and in contrast to aircraft, is that they have many different sensors distributed on their bodies and aerodynamic surfaces, as well as having localized sensory organs such as eyes, ears, and inertial sensors. Insects have many flow-sensitive hairs distributed about their bodies, as well as strain-sensitive campaniform sensilla distributed throughout their wings [8]. Birds have thousands of mechanoreceptors throughout their wings [9], which are thought to encode airflow information [10], while also having proprioceptive muscle spindles that give them information about the positions of the different parts of their bodies and the forces acting on these [11]. Similarly, bats have flow-sensitive hairs all over their wings [12], as well as very similar proprioceptors to birds. Overall, these types of distributed sensors, where the sensors are located at many different points spatially, provide animals with a rich suite of sensory input about the spatial distribution of airflow and loading over their bodies and wings; and it would appear that these distributed sensory systems play an important role in their robust and efficient flight control. This offers bioinspiration for the development of multimodal distributed sensor arrays for aircraft flight control.

The development of distributed airflow sensor systems is a growing research area. Distributed flow sensors have been used in flush air data systems in a number of high-performance aircraft, such as the X-33 [13] and the space shuttle [14], where traditional air data booms were impractical. However, these distributed airflow sensors are also increasingly being developed for small unmanned aerial vehicles (UAVs) [15] where there is a need for more agile flight control when flying in cluttered turbulent environments. These systems have used a number of different types of sensors such as diaphragm-based pressure

Presented as Paper 2019-1934 at the AIAA Scitech 2019 Forum, San Diego, CA, January 7–11, 2019; received 29 September 2020; revision received 0 ; accepted for publication 29 September 2020; published online Open Access 5 November 2020.

*Research Associate, Department of Aerospace Engineering; s.araujoestrada@bristol.ac.uk.

†Lecturer in Aerodynamics, Department of Aerospace Engineering.

sensors [16], hot film sensors [17], and artificial hair sensors [18]. Studies of these systems in wind-tunnel testing, as well as flight testing [19,20], have shown the potential of these systems for measuring a range of aerodynamic parameters.

The use of distributed force or strain measurement for flight control is a less well-investigated area than distributed flow sensing. Initial work has shown the potential for this type of sensor information to improve flight control, with the potential for faster responses [21] and the use of a physics-based control approach [22]. Previous studies have looked at the advantages of each system in isolation in separate aircraft [23] but, as yet, the potential advantages of using both distributed airflow and load information in a single aircraft have not been well explored.

The contribution of this work is to investigate how distributed pressure and strain information can be used together to estimate aerodynamic variables and loads, including in highly unsteady conditions such as stall, with a view of using these different sensory modalities together as real-time inputs for flight control for small-scale fixed-wing UAVs. As part of this, we investigate whether a linear estimation approach is suitable for extracting information from a distributed sensor array or whether a nonlinear estimation approach is required.

This paper is organized as follows: Sec. II presents the experimental methods and platforms used for this research and their main characteristics. Section III presents results from wind-tunnel tests carried out to characterize the strain and pressure signals. Section IV presents aerodynamic variables and loads prediction results using strain and pressure experimental data. Section V summarizes the information presented in this paper, and it discusses areas of potential application for distributed sensing. Lastly, Sec. VI presents some concluding remarks.

II. Experimental Platform Description

A. Wing Model

A wind-tunnel wing model with distributed arrays of both strain sensors and pressure sensors was constructed using the main wing of a radio control aircraft model (Ripmax model WOT4 Foam-E Mk2+, Enfield, England, United Kingdom). The wing airfoil section was a custom shape and had not previously been aerodynamically characterized. The wing had a rectangular planform, with a wingspan of $b = 1.205$ m and a chord of $c = 0.25$ m. Only half of the wing was used for the model; i.e., the wind-tunnel model wingspan was 0.602 m. A total of 30 pressure sensors located in the fuselage were connected to corresponding pressure ports in the wing. The ports were distributed along the wing chord and installed in two different locations along the span using three-dimensionally (3-D)-printed inserts. The chordwise location of the pressure ports is shown in Fig. 1a, whereas the spanwise location of the 3-D inserts is shown in Fig. 1b. The pressure port locations were labeled LE for the leading edge, T01 to T07 for top surface ports one to seven, and B01 to B07 for bottom surface ports one to seven. To differentiate ports between sections, a hyphenated label is employed: for instance ports LE-A, T03-B, and B07-A should be interpreted as leading-edge section A, top surface port-three section B, and bottom surface port-seven section A, respectively. This arrangement provided information on the chordwise pressure distribution of the wing at two locations along the span. An array of 16 strain gauges was installed on the wing spar, an aluminum beam located at the quarter-chord of the wing. The strain gauges were divided into four subarrays, with each subarray able to measure the vertical bending moment and torsional strain. Figure 1b shows the spanwise location of each strain gauge subarray, with SG-A, SG-B, SG-C, and SG-D denoting the strain gauge arrays in locations A to D, respectively. Note that all experiments were carried out in a cantilever configuration, i.e., fixed condition at the wing root and free at the wing tip. Dual-grid strain gauge pairs were used to measure strain due to bending moment. At each location, two opposing pairs were installed in a full-bridge configuration on the beam surface: one on top and another on the bottom. Triaxial strain gauge rosettes were used to measure strain due to torsional moment. At each location, two opposing rosettes were installed in a full-bridge configuration on the beam surface: one on each side of the beam. The full-bridge configuration provided temperature compensation and the highest output sensitivity. Calibration experiments were carried to compute the vertical bending moment from the corresponding strain measurement. With the wing in a cantilever beam configuration, point loads ($PL = [1.96, 3.92, 5.89, 7.85, 9.81]$ N) were applied to the wing tip at $\alpha = [-30, -20, -10, 0, 10, 20, 30]$ deg. The resulting dataset was used to compute calibration factors for each strain gauge. The sensor technical specifications are given in Table 1. Higher range pressure sensors were used in parallel with lower range sensors for some ports where there was potential for the sensors to saturate, with their signals fused in the data processing stage. The fused sensor signal was computed using the following expression:

$$P_s = \begin{cases} P_a & \text{if } P < 460.0 \text{ Pa} \\ 0.8P_a + 0.2P_b & \text{if } 460.0 \text{ Pa} \le P < 480.0 \text{ Pa} \\ P_b & \text{if } P \ge 480.0 \text{ Pa} \end{cases}$$

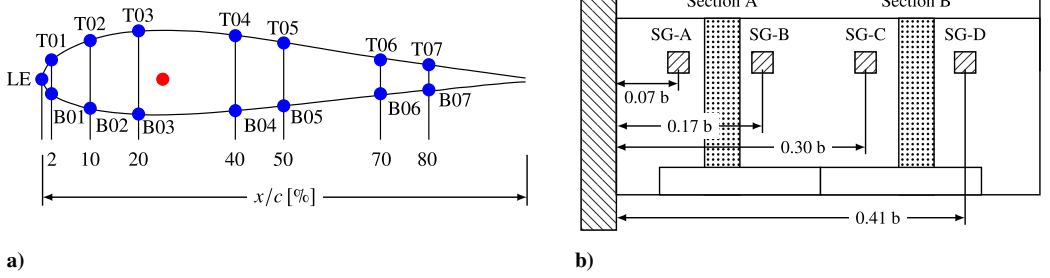

a) b)

Fig. 1 Wing model experimental platform sensor locations: a) chordwise pressure array distribution, and b) spanwise strain array distribution.

Table 1 Wing model experimental platform sensor technical specifications

	Sensor features			
	Static pressure	Static pressure	Vertical bending	Torsion
Model	SDP36	MPXV7002	SGD-2/350-DY13	SGD-2/350-RY53
Manufacturer	Sensirion	Freescale Semiconductor	Omega Engineering	Omega Engineering
Measurement range	±500 Pa	±2 kPa	±30,000 μm/m	±30,000 μm/m

where P_s is the fused pressure signal, P_a is the low measurement range sensor signal, P_b is the high measurement range sensor signal, and P represents the actual pressure. The wing model was fitted with two servo motors to drive the motion of the wing control surfaces. A pitot tube was installed on the wing to provide auxiliary airspeed readings. Figure 2 shows a photograph of the wing model experimental platform distributed sensing array layout and the model when installed in the wind tunnel.

B. One-Degree-Of-Freedom Pitch Rig

The wing model was mounted on a one-degree-of-freedom (1-DOF) pitch motion wind-tunnel rig, with the motion driven by a servo motor (Schneider Electric model LXM32MD30M2, Rueil-Malmaison, France). Figure 3a shows a schematic representation of the 1-DOF pitch motion wind-tunnel rig layout. The aerodynamic loads were measured using a load cell (ATI Industrial Automation model Mini 45, Apex, North Carolina) mounted at the interface between the wing support and the rig's shaft. Note that as the load cell rotated together with the wing, the measured loads were in the body axes system and later transformed to inertial axes (wind-tunnel system) in postprocessing. A timing pulley-belt system connected the rig's shaft to a magnetic rotary encoder (Renishaw model RMB20SC, Wotton-Under-Edge, Gloucestershire, England, United Kingdom). This sensor provided measurements of the angle of attack. The rig's shaft was connected to the servo motor through an elastomer insert coupling (R+W model EKH-60-B-24-28, Klingenberg, Germany).

C. Data Acquisition System

A custom data acquisition (DAQ) system, including custom-built hardware, was used to collect pressure, strain, aerodynamic loads, and aerodynamic variables data. Figure 3b shows a block diagram of the DAQ system. The DAQ system was divided into seven microcontroller unit (MCU)-based subsystems:

1) The section A subsystem acquired the signals from the pressure sensors in the section A insert and the SG-A and SG-B strain gauge arrays; it also received and stored data from the rig control electronics and controlled the inboard servo motor.

2) The section B subsystem acquired the signals from the pressure sensors in the section B insert and the SG-B and SG-C arrays, and it controlled the outboard servo motor.

3) The rig control electronics subsystem acquired the angle-of-attack rig encoder signal and was used as an alternative system to control the motion of the rig's servo.

4) The central MCU subsystem received time-stamped data acquired by section A, section B, and rig control electronics subsystems; and it transmitted it to a PC via Universal Serial Bus (USB) communication.

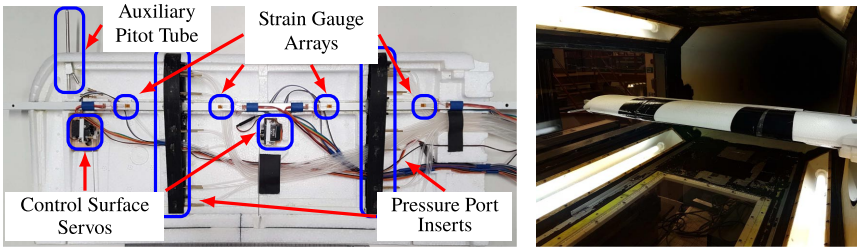

Fig. 2 Wing model experimental platform: a) distributed sensing array on wing, and b) model installed in wind tunnel.

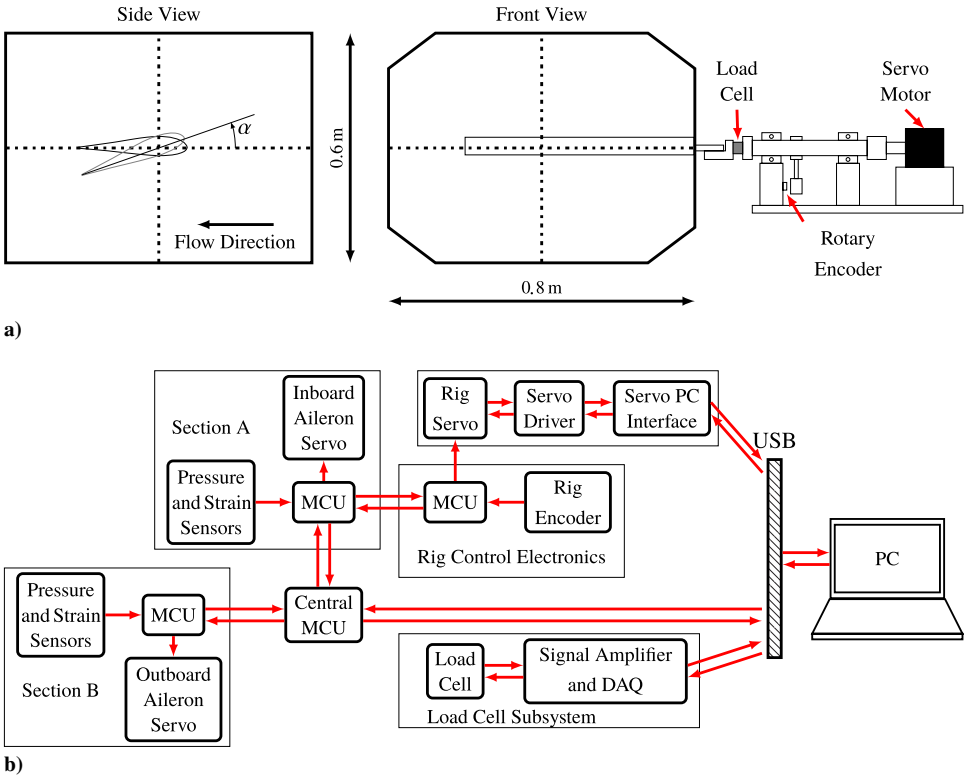

Fig. 3 Pressure and strain sensing experimental platform: a) wind-tunnel layout, and b) DAQ system.

This subsystem could also be used to transmit commands generated by the PC to the other subsystems.

5) The load cell subsystem measured, acquired, conditioned, and transmitted load signals to the PC via USB using a multifunction I/O device (National Instruments model USB-6218, Austin, Texas).

6) The PC collected and stored pressure, strain, aerodynamic loads, and aerodynamic variables data.

7) Lastly, the rig servo subsystem controlled the motion of the servo. The servo motor motion commands could be generated by the PC using proprietary software (Schneider Electric SoMove, Rueil-Malmaison, France) or by the rig control electronics MCU, which allowed for automatically generated inputs or tracking of an external analog signal.

All acquired data were sampled at 200 Hz by the appropriate subsystem and received by the PC. It was then routed using user datagram protocol messages and stored on disk by a custom graphical user interface written in Python. A simple network time protocol (SNTP) was used to synchronize the clock signal of the MCU subsystems with the PC clock signal. The SNTP implementation achieved a maximum time offset of less than 1.0 ms between clock signals. Results from a series of characterization experiments are presented in the next section.

III. Signal Characterization Results

Using the wing model and testing rig described in Sec. II, a series of characterization experiments were carried out in the University of Bristol's low-turbulence wind tunnel [24]. Quasi-static as well as dynamic tests were performed at airspeeds of $V = [8, 10, 12, 14, 16, 18, 20]$ m/s to characterize the aerodynamic loads, pressure, and strain signals. These tests consisted of α sweeps at various pitch rates. The data collected from these tests were used to identify stall characteristic markers in measured pressure and strain signals, as well as to acquire datasets for estimation of airspeed V, angle of attack α, lift L, drag D, and pitching moment M, as well as the characteristic response of the signals to changes in pitch rate q.

At the beginning of each experiment, $\alpha = 0$ deg was held; then, α was decreased until $\alpha = -15$ deg was reached. Then, the direction of the sweep was changed and the motion continued until $\alpha = 20$ deg was reached. The direction of the sweep was then changed until $\alpha = -15$ deg was reached, and this cycle was repeated four more times. Lastly, at the end of the fifth cycle ($\alpha = 20$ deg), the direction of the sweep was changed once more until $\alpha = 0$ deg was reached and the experiment ended. During each α sweep, the corresponding q was held constant. Sweeps with $q = [0.1, 0.5, 5, 10, 20, 30, 40, 50]$ deg/s were performed. No significant dynamic effects were observed between datasets for $q = [0.1, 0.5, 5]$ deg/s; therefore, data corresponding to $q \leq 5$ deg/s were considered as quasi static in the following analysis.

Figure 4 shows the characteristic response signals against α from selected pressure and strain sensors in the distributed sensing array for an experiment with $V = 20$ m/s at various pitch rates, with all five sweeps for each pitch rate overlaid. For ease of interpretation, the data in these plots are presented in normalized form with the measured signals computed as follows:

$$C_{P_i} = \frac{P_i - P_\infty}{(1/2)\rho V^2} \tag{1}$$

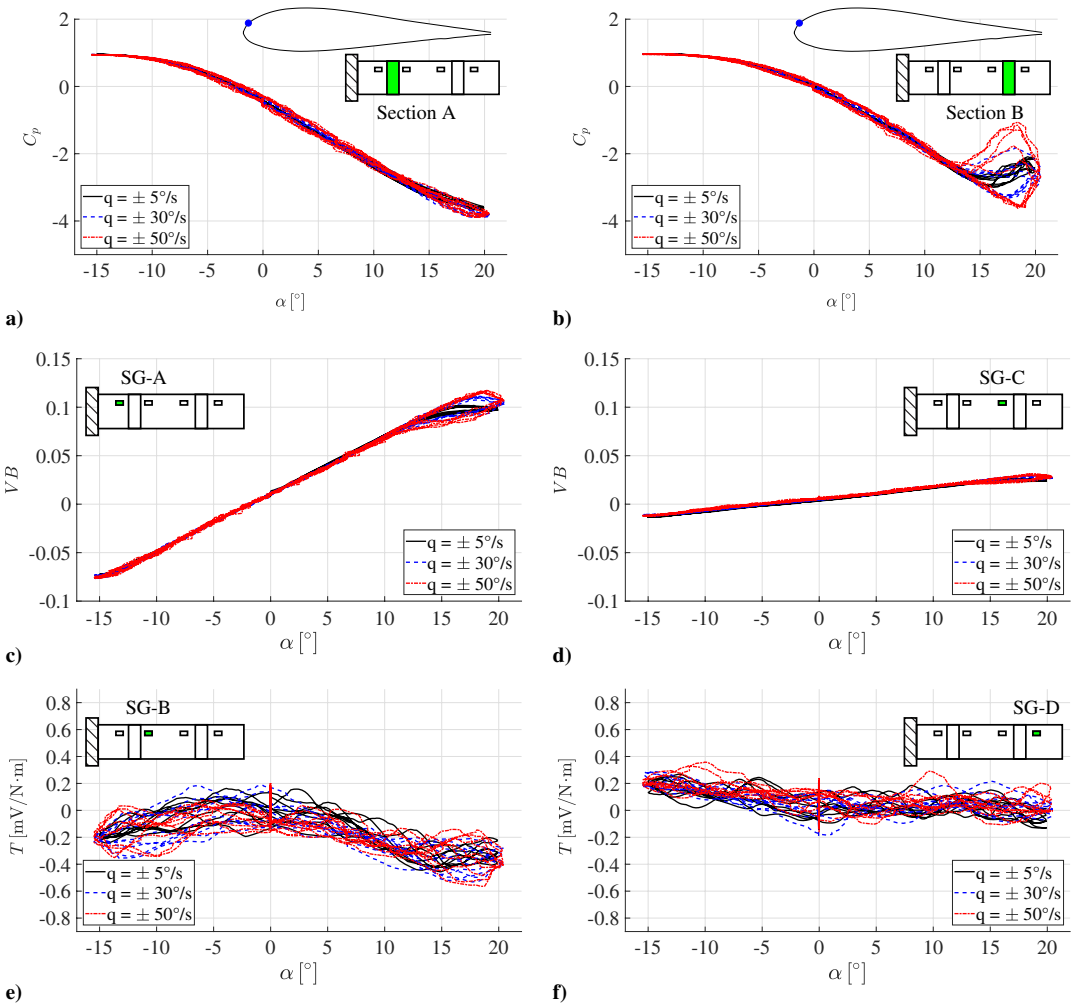

Fig. 4 Distributed sensing array signal variation with α at various q with $V = 20$ m/s: a) $C_{P_{T01\text{-}A}}$, b) $C_{P_{T01\text{-}B}}$, c) $VB_{SG\text{-}A}$, d) $VB_{SG\text{-}C}$, e) $T_{SG\text{-}B}$, and f) $T_{SG\text{-}D}$.

$$VB_j = \frac{BM_j}{(1/2)\rho V^2 Sc} \tag{2}$$

$$T_j = \frac{TS_j}{(1/2)\rho V^2 Sb} \tag{3}$$

where P_i is the pressure signal from sensor i, BM_j is the bending moment signal from sensor j, and TS_j is the torsional strain signal from sensor j with

$$i = \text{LE-A, T01-A, } \ldots \text{, T07-A, B01-A, } \ldots \text{, B07-A,}$$
$$\text{LE-B, T01-B, } \ldots \text{, T07-B, B01-B, } \ldots \text{, B07-B}$$

and $j =$ SG-A, SG-B, SG-C, and SG-D (see Fig. 1 for sensor locations).

Figures 4a and 4b show $C_{P_{\text{T01-A}}}$ and $C_{P_{\text{T01-B}}}$ variations with α (both located at $0.1c$). $C_{P_{\text{T01-A}}}$ behaves in a parabolic fashion for -15 deg $\leq \alpha \leq 15$ deg, with approximate linear behavior for -5 deg $\leq \alpha \leq 10$ deg. Note, however, that hysteretic behavior can be observed in this region for $q = 50$ deg/s. For -15 deg $\leq \alpha \leq 15$ deg, $C_{P_{\text{T01-B}}}$ also behaves in a parabolic fashion but with a reduced linear behavior. Hysteretic behavior can be observed in this region for $q = 50$ deg/s. Evidence of flow detachment can be observed for $C_{P_{\text{T01-B}}}$ at $\alpha > 12$ deg. Both signals display hysteretic behavior for the $q = [30, 50]$ deg/s datasets: for $C_{P_{\text{T01-A}}}$, this behavior is seen in 15 deg $\leq \alpha \leq 20$ deg; whereas for $C_{P_{\text{T01-B}}}$, the region expands to 12 deg $\leq \alpha \leq 20$ deg.

Figures 4c and 4d show $VB_{\text{SG-A}}$ and $VB_{\text{SG-C}}$ variations with α, respectively. Linear behavior is observed for $VB_{\text{SG-A}}$ in -12 deg $\leq \alpha \leq 10$ deg; whereas for $VB_{\text{SG-C}}$, the linear region expands to -15 deg $\leq \alpha \leq 15$ deg. Hysteretic behavior is observed for $VB_{\text{SG-A}}$ for the $q = [30, 50]$ deg/s datasets in 12 deg $\leq \alpha \leq 20$ deg. Hysteretic behavior is also observed for $VB_{\text{SG-C}}$ for the $q = 50$ deg/s dataset in 15 deg $\leq \alpha \leq 20$ deg. Figures 4e and 4f show $T_{\text{SG-B}}$ and $T_{\text{SG-D}}$ variations with α. Both signals display noisy and highly nonlinear variation with α.

The results presented in this section show that there is a wealth of information available in the pressure and strain signals. Flow visualization pilot experiments suggest that the pressure signals could be used to estimate the state of the flow around the wing, showing whether the flow is attached, detaching, or detached. The signals also capture the nonlinear behavior that occurs around stall and at high pitch rates. And lastly, in combination with inertial data q, the signals capture the hysteretic behavior of the system, offering the potential to take advantage of dynamic lift and related effects. These characteristics can be estimated using the information from the distributed array. In the next section, an example application using the distributed array data to estimate the values of aerodynamic variables and loads is presented.

IV. Aerodynamic Variables and Loads Prediction

Using data from the quasi-static and dynamic experiments presented in Sec. III, the values of aerodynamic variables and loads were estimated using two approaches: one based on an artificial neural network (ANN) and another based on a partial least-squares (PLS) regression estimator. These two methods were chosen to evaluate the level of complexity required for estimation of the aerodynamic variables and loads, with a simple linear estimator given by PLS and a complex nonlinear estimator provided by an ANN. Here, ANN estimators are nonlinear estimators where layers of interconnected artificial neurons with nonlinear activation functions are optimized to estimate desired output variables based on a set of training data containing measured input data and the corresponding output. Provided the right structure and parameters are selected, ANNs have been proven to be universal approximators [25]. On the other hand, PLS estimation is a linear estimation method where a series of linear combinations of the input predictor variables (components) are calculated based on maximizing their covariance with the output response variable [26]. The method can be thought of as a combination of multiple linear regression and principal component analysis.

To assess the significance of each dataset when estimating the aerodynamic variables and loads, a three-level classification of estimators was defined. This classification is based on the available data and the conditions under which the experiments were performed. Figure 5 shows the classification used to define the estimators. The first classification level is defined by the type of training data used for the estimation. There are two sets in this level: quasi-static and dynamic training data. The second classification level is defined by the availability, or not, of inertial data as input; i.e., the measured q is fed, or not, into the estimator. Lastly, the estimators are divided into one of five subsets, depending on the data from the distributed array used as input for estimation: vertical strain (VS), vertical-torsional strain (VTS), pressure (P), pressure-vertical strain (PVS), and pressure-vertical-torsional strain (PVTS). Hence, "quasi-static IVS" denotes a dataset using both quasi-static and inertial data as well as the vertical strain signals from the distributed array, "dynamic IPVTS" denotes a dataset using dynamic and inertial data as well as the pressure, vertical strain and torsional strain signals from the distributed array, whereas "dynamic P"

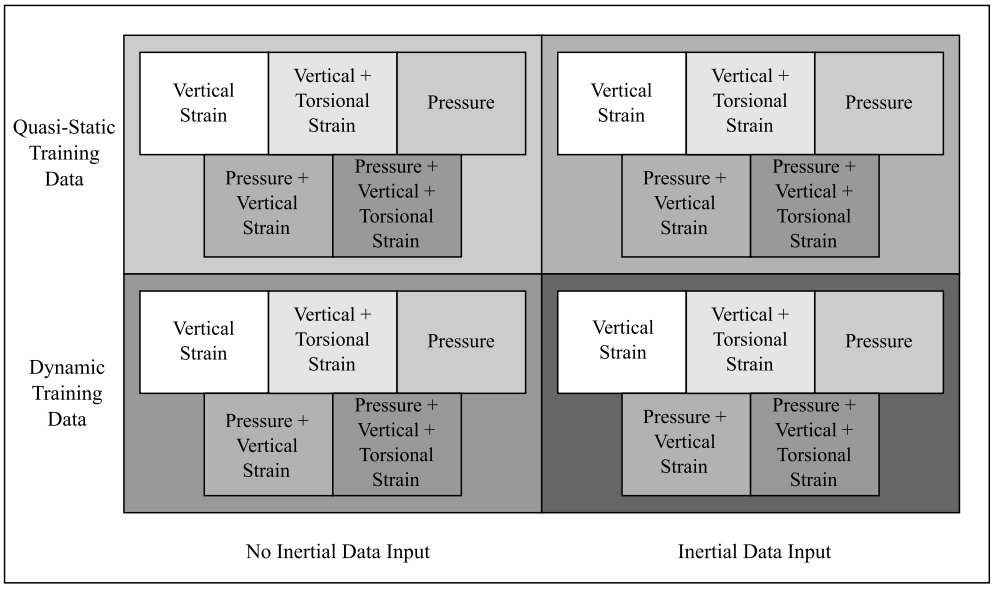

Fig. 5 Aerodynamic variables and loads estimators classification.

denotes a dataset using dynamic data as well as the pressure signals from the distributed array but no inertial data.

To assess the performance of each estimator class, the experimental data were divided into three sets: the validation, quasi-static training, and dynamic training sets. The dataset separation is defined next and shown in Fig. 6. The validation set consists of datasets for $q = [10, 20, 40]$ deg/s and $V = [8, 10, 12, 14, 16, 18, 20]$ m/s, as well as datasets with $V = [10, 14, 18]$ m/s and $q = [5, 30, 50]$ deg/s. The quasi-static training set used data with $V = [8, 12, 16, 20]$ m/s and $q = 5$ deg/s. Lastly, the dynamic training set used data with $V = [8, 12, 16, 20]$ m/s and $q = [5, 30, 50]$ deg/s.

A. Estimators Structure

The general structure of the ANN used for the estimation of aerodynamic variables and loads is shown in Fig. 7a. All the trained ANNs consisted of three layers: the input, hidden, and output layers. The input layer handled the inputs to the ANN; it conditioned the input signals to improve the likelihood of successfully training an ANN by scaling them using the minimum value and range of the expected inputs. The inputs were fed into the ANN in the following units: pressure in pascals, vertical bending moment in newton meters, and torsional moment in millivolts. The output from each of the neurons in this layer was defined as

$$a_i^{[1]} = \frac{2[x_i - \min(x_i)]}{\max(x_i) - \min(x_i)} - 1 \tag{4}$$

with x_i representing the ith input signal to the ANN of a total of $N^{[1]}$ signals. Note that the input layer is numbered as layer "1".

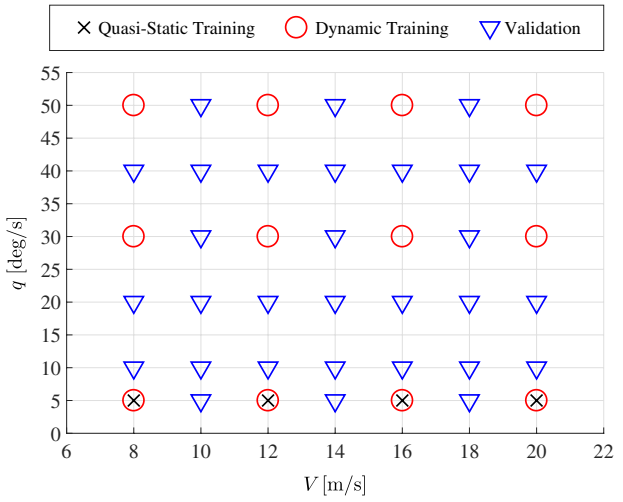

Fig. 6 Datasets' definition for aerodynamic variables and loads estimation.

The hidden layer consisted of interconnected artificial neurons with the output of the jth neuron in layer $\ell (\ell = 2, \ldots, L)$ defined by

$$a_j^{[\ell]} = g^{[\ell]}\left(\sum_{k=1}^{N^{[\ell-1]}} w_{jk}^{[\ell]} a_k^{[\ell-1]} + b_j^{[\ell]}\right) = g^{[\ell]}(z_j^{[\ell]}) \tag{5}$$

with $b_j^{[\ell]}$ as the bias term for the jth neuron $(j = 1, \ldots, N^{[\ell]})$, $a_k^{[\ell-1]}$ as the output of the kth neuron in layer $\ell - 1 (k = 1, \ldots, N^{[\ell-1]})$, $w_{jk}^{[\ell]}$ as the weight value for the jth neuron given to the output of the kth neuron in layer $\ell - 1$, and $g^{[\ell]}(z_j^{[\ell]})$ as the activation function of the jth neuron. All the neurons in the hidden layers used hyperbolic tangent sigmoid functions as activation functions.

Lastly, the output layer took the signals produced by the hidden layer and scaled them to match the magnitude of the target function. The output from this layer is defined by

$$\hat{Y} = k a^{[L]} \tag{6}$$

with k as a scaling factor, and $a^{[L]}$ as the output from the hidden layer L.

To find the best estimator for each estimator class, a direct search was performed where a total of 32 ANNs with different numbers of neurons and hidden layers were trained to estimate either α, V, D, L, or M. A weighted sum of the mean-square error for training and validation was used as selection criteria to find the ANN that best fit the data. The ANNs were trained using MATLAB Version 9.2 and Neural Network Toolbox Version 10.0, Release 2017a (MathWorks, Inc., Natick, Massachusetts), employing the Levenberg–Marquardt backpropagation algorithm as the training function. The characteristics of the selected ANN-based estimators are given in Table 2.

While training the ANN-based estimators, a significant variance in results for D and L was found when the quasi-static plus inertial dataset was used for training. This variance appeared to be due to sensitivity to the randomized initial ANN weights and biases. This effect was explored by performing 10 independent training runs for each dataset. All five estimation classes based on the sensing combination were assessed, i.e., VS, VTS, P, PVS, and PVTS. For each training run, 32 different ANN structures were trained, each with a different number of layers and neurons, keeping the best one for each class. This produced 10 ANN-based estimators for each sensing combination. This analysis confirmed that the variance in results was due to random initial conditions and that it only affected the ANN-based D and L estimators trained using the quasi-static plus inertial dataset. In the following analysis, the median root-mean-square-error (RMSE) estimation value computed from the 10 independently trained ANN-based estimators is used to perform a fair assessment between estimators.

The general structure of the PLS-based estimator used for the estimation of aerodynamic variables and loads is shown in Fig. 7b. The main benefits of PLS-based estimation are that it provides an

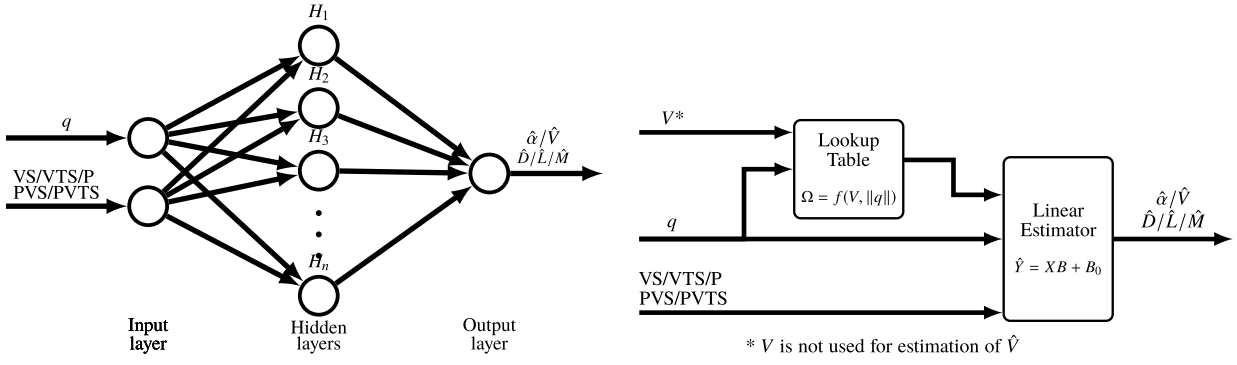

a) b)

Fig. 7 General structure of aerodynamic variables and loads estimators: a) ANN and b) PLS.

Table 2 Characteristics of ANN-based estimators

	ANN characteristics			
Variable	Class	No. of layers[a]	No. of nodes[a]	Structure
α, deg	Dynamic IPVS	5	22	[7,6,5,3,1]
V, m/s	Dynamic P	4	10	[3,3,3,1]
D, N	Dynamic IPVTS	2	9	[8,1]
L, N	Dynamic IPVTS	4	19	[7,6,5,1]
M, N · m	Dynamic PVTS	3	11	[7,3,1]

[a]Excludes input layer.

estimator that is quick to obtain/train, is the most representative linear mapping between input and output, is compact (low memory requirements), is computationally inexpensive (fast to compute), and is relatively easy to implement. The PLS-based estimator consists of a lookup table block and a linear estimator block. The lookup table block takes V and q as inputs and returns a vector of weights defined by the surface $\Omega = f(V, \|q\|)$. Any query point not contained in the table is either interpolated or extrapolated, using a cubic spline method, depending on whether the query point lies within the domain or not. In the linear estimator block, the vector of weights is then used in combination with the distributed array signals $X = \text{VS/VTS/P/PVS/PVTS}$ to produce an estimate of the aerodynamic variables and loads $\hat{Y}$. Note that V is not used for the computation of $\hat{V}$, and that X is fed into the linear estimator in the following units: pressure in pascals, vertical bending moment in newton meters, and torsional strain signal in millivolts.

The surface Ω in the lookup table block was built by carrying out PLS regression using all of the points in the data training set defined in Sec. IV. The PLS regression computes a predictor defined by

$$y_i = \sum_{j=1}^{N} x_j b_{ij} + b_{i0} \tag{7}$$

which is a linear combination of the input vector X with size N (defined by input set, i.e., VS/VTS/P/PVS/PVTS) and weights vector $B_i = b_{i0}, \ldots, b_{iN}$, with y_i as the target output vector (α, V, D, L, or M) and with each individual experimental condition represented by i, from a total of O conditions used for the PLS regression. Finally, Ω is formed by collecting all of the B_i vectors. The PLS regression was performed using the *plsregress* algorithm in MATLAB Version 9.2, Release 2017a (MathWorks, Inc., Natick, Massachusetts). The number of components was changed, depending on the number of signals from the distributed array used as input, as a compromise between the available number of signals (four components for VS) and a representative enough set of components (eight components for VTS, P, PVS, and PVTS).

B. Estimators Comparison

The results of the ANN-based estimation of α and L are presented next as representative cases. Figure 8 shows the α and L estimation RMSE variation between estimator classes for the validation dataset. In each plot, the RMSE data are first grouped by training dataset into quasi-static (QS), quasi-static plus inertial (QS + inertial), dynamic (DYN), and dynamic plus inertial (DYN + inertial). Then, the type of data used as input for estimation is indicated along the x axis, with the number of sensor signals increasing from left to right (from VS to PVTS). Figure 8a shows the overall RMSE variation for α estimation. The first feature that stands out is that strain-data-only-based estimators (VS and VTS) perform very poorly within each of the four subclasses when used to estimate α, with the overall validation RMSE value greater than 2.0 deg; and, when poststall ($\alpha > 10$ deg) performance is considered (Fig. 8b), the RMSE doubles in value, with the minimum RMSE greater than 4.0 deg. A second aspect to notice is that the availability of q data does not seem to improve the performance of any of the α estimators significantly, with minimal improvement being seen in any case. In general, when considering the quasi-static dataset results, including inertial data slightly increases the α RMSE for all sensor combinations (Fig. 8a); this is also the case for conditions where $\alpha > 10$ deg (Fig. 8b). In contrast, for the dynamic dataset results, including inertial data decreases the α RMSE (Fig. 8a). For conditions where $\alpha > 10$ deg, RMSE variation between estimators is significantly smaller and difficult to attribute to the availability of inertial data alone. However, the addition of inertial data seems to decrease the RMSE. Third, when α estimators trained with quasi-static data are compared against the matching estimators trained with dynamic data, there is a significant performance improvement

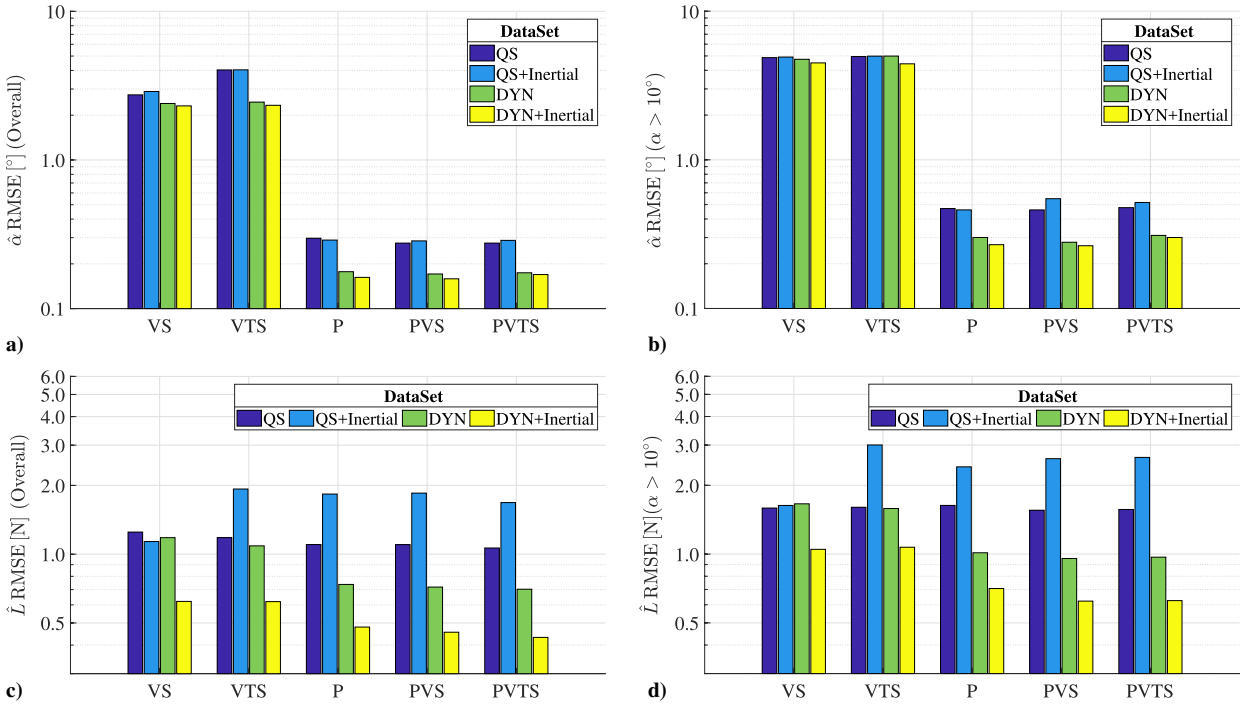

Fig. 8 Validation RMSE variation between ANN estimators: a) overall $\hat{\alpha}$ RMSE, b) $\hat{\alpha}$ RMSE for $\alpha > 10$ deg, c) overall $\hat{L}$ RMSE, and d) $\hat{L}$ RMSE for $\alpha > 10$ deg. Estimator notation defined in Fig. 5. (Note logarithmic RMSE axis scale.)

in validation performance. For instance, if VS- and VTS-based estimators are not considered, the RMSE of the remaining estimators in the dynamic class is smaller than 0.2 deg (Fig. 8a), with the poststall RMSE value approximately increasing to 0.3 deg (Fig. 8b); in comparison, quasi-static trained estimators having overall and poststall RMSE values of approximately 0.3 and 0.5 deg, respectively. Based on the overall estimation RMSE as the selection metric, the PVS estimator trained with dynamic and inertial data is the best estimator for α (Fig. 8a).

Figure 8c shows the overall RMSE variation for L estimation. The first feature that stands out is that the availability of inertial data decreases the performance of almost every estimator trained using the quasi-static dataset. This is thought to be caused by the estimator class overfitting to the training data, which does not include the full range of q values included in the validation dataset (see Fig. 6). In contrast, availability of q significantly improves the performance of the estimators trained with the dynamic dataset. Second, if estimators trained with quasi-static plus inertial data are not considered, progressive improvement within each L estimator class is observed as more input signals are used. Note that the P-, PVS-, and PVTS-based estimators significantly improve in performance as complexity increases. Third, the VS- and VTS-based estimators do not perform as poorly as the ones for α estimation but are still the worst performing within each estimator class. Fourth, the estimators in the dynamic training data class perform better than those in the quasi-static training data class. For instance, the worst-performing estimators in the dynamic class (maximum RMSE $\approx$1.18 N) achieved a similar performance level as the best-performing estimators in the quasi-static class (Fig. 8c). The performance trend holds for poststall conditions ($\alpha > 10$ deg), with the worst-performing dynamic estimator RMSE $\approx$1.66 N being similar to the average RMSE of the quasi-static training data class (Fig. 8d). Overall, increasing the type of input data decreases the L RMSE for all sensor combinations for the quasi-static as well as the dynamic datasets (Fig. 8c). Based on the overall estimation RMSE as the selection metric, the PVTS trained with dynamic and inertial data is the best L estimator (Fig. 8c).

Based on the findings for the ANN-based estimators described earlier in this paper, a comparison between ANN-based and PLS-based estimators is presented next. All the estimators considered in the comparison were trained using the dynamic plus inertial dataset because this input set is the one that provided the best results. Figure 9 shows the overall validation RMSE variation of ANN-based and PLS-based estimators for α in Fig. 9a and L in Fig. 9b. When considering the strain-data-only estimators (VS and VTS), PLS-based ones perform better than ANN-based ones. However, once any combination containing pressure data is included, ANN performs better than PLS. In general, the performance of ANN-based estimators improves with an increase in the type of input data. In contrast, increasing the type of input data does not improve the performance of the PLS-based estimators. In fact, the performance seems to be bounded by the performance of the best independent signal; for instance, for α estimation, PVS and PVTS performances are equal to P. Overall, ANN estimators outperform PLS estimators here. For ANN-based α, the best RMSE is 0.159 deg (PVS), against 0.525 deg (PVS) for the PLS-based estimator. For ANN-based L, the best RMSE is 0.432 N (PVTS), against 0.642 N (PVS) for the PLS-based estimator.

The levels of error of the estimators presented here are comparable to previously published work. For instance, for α estimation, experiments using arrays of sensors mounted on wings in prestall conditions have achieved errors ranging from 1.80 [27] to 0.26 deg [28]; whereas for L estimation, RMSE values of 0.105 N [18] have been reported. The RMSE performance variation for V, D, and M estimators was similar to the reported performance of the α estimators. A detailed comparison between the two types of estimators for both α and L is presented in the following subsections.

C. Angle-of-Attack Estimation Comparison

Based on the estimation performance presented in Sec. IV.B, the best ANN-based and PLS-based α estimators are selected for comparison. Both estimators belong to the PVS class and were trained using dynamic examples and inertial information. In the following discussion, α and L represent actual measurements (i.e., signal readings from an encoder and a load cell respectively), and $\hat{\alpha}$ and $\hat{L}$ represent estimates of α and L. For the dynamic pitch case, the local α is influenced by q. The change in local α due to q can be approximated by the following expression:

$$\Delta\alpha = \frac{q\ell\cos\alpha}{V + q\ell\sin\alpha} \tag{8}$$

where ℓ is the distance between the rotation point and a point on the surface of the wing, and V is the wind speed. In Eq. (8), $q\ell$ represents the tangential speed due to the circular motion at speed q. It follows that the terms $q\ell\cos\alpha$ and $q\ell\sin\alpha$ represent the vertical and horizontal components of the tangential speed projected into the wind axes frame. Then, for a given ℓ, Eq. (8) has a maximum when $\alpha = 0$, q is at its maximum absolute value, and V is at its minimum. For the experimental data presented here, and with $\ell = 0.138$ m (furthermost pressure tap location), $q = 50$ deg/s, and $V = 8$ m/s, this value is approximately 0.86 deg. Note that this value represents an upper bound on $\Delta\alpha$ for the furthermost pressure tap location and that the change in local α for the remaining locations is smaller. Due to this small effect, the unmodified encoder measurement was used directly when computing the baseline α for all the dynamic pitch cases.

Figure 10 shows $\hat{\alpha}$ against the nominal α (encoder measurement) with $V = 18$ m/s for both quasi-static and dynamic datasets. Figure 10a shows a comparison between α and $\hat{\alpha}$ computed using an ANN-based estimator, when quasi-static data are used as input. The black plus sign (+) markers represent the measured α, and the red dot ($\cdot$) markers represent the PVS estimator output. The performance of the PVS ANN-based estimator is satisfactory throughout the α range, with the two point clouds lying one on top of the other. The detailed plot in Fig. 10a shows that this trend holds even at high α (10 deg $\leq \alpha \leq$ 20 deg). Figure 10b shows a comparison between α and $\hat{\alpha}$ when dynamic data are used as input for the ANN-based estimator. The performance of the PVS ANN-based estimator is satisfactory throughout the α range, with no signs of hysteretic behavior effects (even in the 14 deg $\leq \alpha \leq$ 20 deg region) overlaying the α signal measured by the encoder. Figure 10b shows a comparison between α and $\hat{\alpha}$ computed using a PLS-based estimator when quasi-static data are used as input. The black plus sign (+)

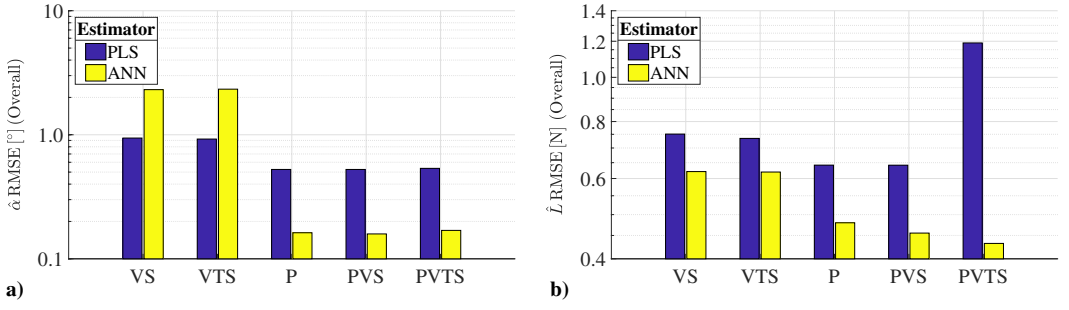

Fig. 9 Overall validation RMSE variation between estimators: a) $\hat{\alpha}$ RMSE and b) $\hat{L}$ RMSE.

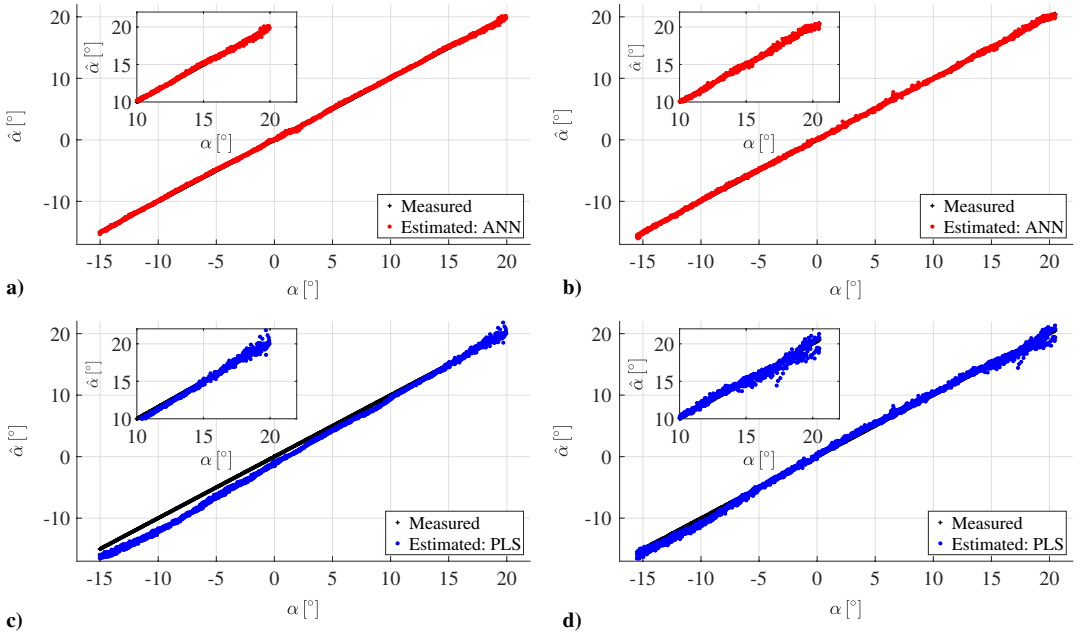

Fig. 10 $\hat{\alpha}$ comparison for $V = 18$ m/s: a) ANN-based with $q = \pm 5$ deg/s, b) ANN-based with $q = \pm 40$ deg/s, c) PLS-based with $q = \pm 5$ deg/s, and d) PLS-based with $q = \pm 40$ deg/s.

markers represent the measured α, and the blue dot $(\cdot)$ markers represent the PVS estimator output. The PVS PLS-based estimator provides a good α estimate, but only for 5 deg $\leq \alpha \leq$ 15 deg. Outside of this region, the estimation is not as good as the ANN-based one, with an important mismatch with respect to the reference measurement for $\alpha \leq 5$ deg. Additionally, at $\alpha \geq 16$ deg, the $\hat{\alpha}$ estimation error increases (detailed plot Fig. 10c). Figure 10d shows a comparison between α and $\hat{\alpha}$ when dynamic data are used as input for the PLS-based estimator. When compared with the quasi-static data case, the performance is improved throughout the α range. However, at high α ($\alpha \geq 14$ deg), the $\hat{\alpha}$ estimation error increases (detailed plot Fig. 10d). An analysis on the characteristics of the estimation error for the estimation of α and V is presented in Sec. IV.E.

D. Lift Estimation Comparison

Based on the estimation performance presented in Sec. IV.B, the best ANN-based and PLS-based L estimators are selected for comparison. The ANN-based estimator belongs to the PVTS class and the PLS-based one to the PVS class, with both estimators trained using dynamic examples and inertial information. Figure 11 shows $\hat{L}$ against the nominal α (encoder measurement) with $V = 18$ m/s for both quasi-static and dynamic datasets. Figure 11a shows a comparison between L (load cell measurement) and $\hat{L}$ computed using an ANN-based estimator, when quasi-static data are used as input, with the black plus sign $(+)$ markers representing the measured L and the red dot $(\cdot)$ markers representing the estimator output. The ANN-based PVTS estimator matches L well throughout the α range, with the two point clouds lying one on top of the other. The detailed plot in Fig. 11a

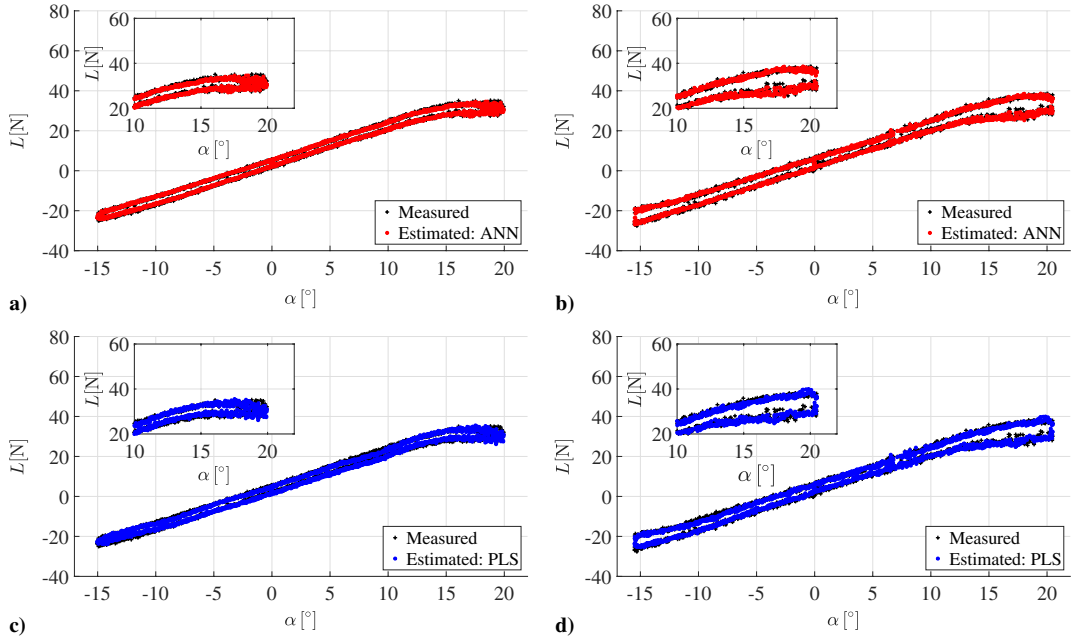

Fig. 11 Lift estimation comparison for $V = 18$ m/s: a) ANN-based with $q = \pm 5$ deg/s, b) ANN-based with $q = \pm 40$ deg/s, c) PLS-based with $q = \pm 5$ deg/s, and d) PLS-based with $q = \pm 40$ deg/s.

shows that the estimation performance remains satisfactory even in the 10 deg $\leq \alpha \leq$ 20 deg region. Figure 11b shows a comparison between L and $\hat{L}$ when dynamic data are used as input for the ANN-based estimator. The estimator is able to correctly reproduce the hysteretic behavior throughout the α range, even for the 10 deg $\leq \alpha \leq$ 20 deg region. Figure 11c shows a comparison between L (load cell measurement) and $\hat{L}$ computed using an PLS-based estimator, when quasi-static data are used as input. With the black plus sign (+) markers representing the measured L and the blue dot (·) markers representing the estimator output. The PLS-based PVS estimator matches L well throughout the α range, with the two point clouds lying one on top of the other, with the estimation performance remaining satisfactory even in the 10 deg $\leq \alpha \leq$ 20 deg region, as shown in the detailed plot in Fig. 11c. Figure 11d shows a comparison between L and $\hat{L}$ when dynamic data are used as input for the PLS-based estimator. The hysteretic behavior is correctly reproduced by the estimator throughout the α range. An analysis of the characteristics of the estimation error for the estimation of D, L, and M is presented in the following subsection.

E. Error Analysis

Using the best performing ANN-based and PLS-based estimators, the RMSE was computed for $\hat{\alpha}$, $\hat{V}$, $\hat{D}$, $\hat{L}$, and $\hat{M}$ for the validation set. The computed RMSE values are given in Table 3, and the RMSE relative to the measurement range (%MR) is shown in brackets.

Figure 12 shows the estimation error distribution for the aerodynamic variables, α and V, for both the ANN-based and the PLS-based estimators when the validation dataset is used as input. In the estimation error vs α plot, for both Figs. 12a and 12b, the edge of the shaded area represents the estimation error range, whereas the × and dot (·) markers are the corresponding estimation error data points. Figure 12a shows the $e_{\hat{\alpha}}$ variation across α and its distribution. The ANN-based estimator error range remains fairly constant across α; this is in contrast with the high degree of variability for the PLS-based estimator error boundary: particularly in both the $\alpha \leq -10$ deg and $\alpha \geq 10$ deg regions. The ANN-based estimator error distribution is significantly better than the PLS-based estimator error distribution, with RMSE = 0.15 deg for the ANN-based estimator and RMSE = 0.53 deg for the PLS-based estimator (Table 3). Note that both error distributions are appreciably different, with the mean value of the ANN distribution centered at $e_{\hat{\alpha}} = 0$ deg, but this is not the case for the PLS error distribution. For instance, the PLS error distribution seems to be positive for $\alpha < 0$ deg, indicating α underprediction for this region. The overall mean PLS error value is slightly negative, indicating overprediction across α.

Figure 12b shows the $e_{\hat{V}}$ boundary across α and the distribution of $e_{\hat{V}}$. The ANN-based $e_{\hat{V}}$ boundary remains fairly constant across α and approximately half as wide as the one for the PLS-based estimator for most of the α range. For $\alpha \geq 10$ deg, the PLS-based estimator $e_{\hat{V}}$ boundary shows an increasing trend with α. The ANN-based estimator error distribution is significantly better than the PLS-based estimator one, with a RMSE of 0.15 m/s against 0.39 m/s. Both error distributions are appreciably different, whereas the ANN distribution is approximately Gaussian; the PLS error distribution is bimodal with a major peak centered at $e_{\hat{V}} \approx 0.2$m/s and a minor one centered at $e_{\hat{V}} \approx -0.2$ m/s. This indicates that the PLS estimator is highly likely to underestimate V by at least 0.2 m/s.

Figure 13 shows the estimation error distribution for the aerodynamic loads, D, L, and M for both the ANN-based and the PLS-based estimators when the validation dataset is used as input. In the estimation error vs α plot for Figs. 13a–13c, the edge of the shaded area represents the range of the estimation error, with the × and dot (·) markers representing the corresponding estimation error data points. The magnitude in each of the plots in Fig. 13 has been normalized by dividing the corresponding quantity by the measurement range (see Table 3). Figure 13a shows the $e_{\hat{D}}$ boundary across α and the distribution of $e_{\hat{D}}$. Both the ANN-based and PLS-based estimators error boundaries show an increasing trend with α, with the $e_{\hat{D}}$ boundary for the ANN-based estimator slightly narrower than the one for the PLS-based estimator. The ANN-based estimator error distribution is very similar to the PLS-based estimator error distribution, with RMSE values for the PLS-based estimator and ANN-based estimator of 0.54 and 0.35 N, respectively. For reference, the measurement range of D was 23.38 N (Table 3). The distribution of $e_{\hat{D}}$ across α for both estimators appears to be very similar; however, the $e_{\hat{D}}$ distribution for the PLS estimator is bimodal with two peaks: one around $e_{\hat{D}} \approx 0.0\%$, and another at $e_{\hat{D}} \approx 3.5\%$. Although the first peak is significantly larger, the existence of the second peak indicates that a number of D estimates will be overpredictions.

Figure 13b shows the $e_{\hat{L}}$ boundary across α and the distribution of $e_{\hat{L}}$. The PLS-based estimator error boundary is wider than the one for the ANN-based estimator across α. Both error boundaries become

Table 3 Error statistics of ANN-based and PLS-based estimators

		RMSE (%MR), overall		RMSE (%MR), $\alpha > 10$ deg	
Variable	Measurement range	PLS	ANN	PLS	ANN
α, deg	35.00	0.525 (1.50)	0.147 (0.42)	0.786 (2.25)	0.243 (0.69)
V, m/s	12.00	0.386 (3.22)	0.148 (1.23)	0.607 (5.06)	0.200 (1.67)
D, N	23.38	0.544 (2.33)	0.351 (1.50)	0.810 (3.46)	0.663 (2.84)
L, N	82.39	0.642 (0.78)	0.438 (0.53)	0.999 (1.21)	0.633 (0.77)
M, N · m	1.29	0.036 (2.80)	0.030 (2.33)	0.058 (4.50)	0.046 (3.57)

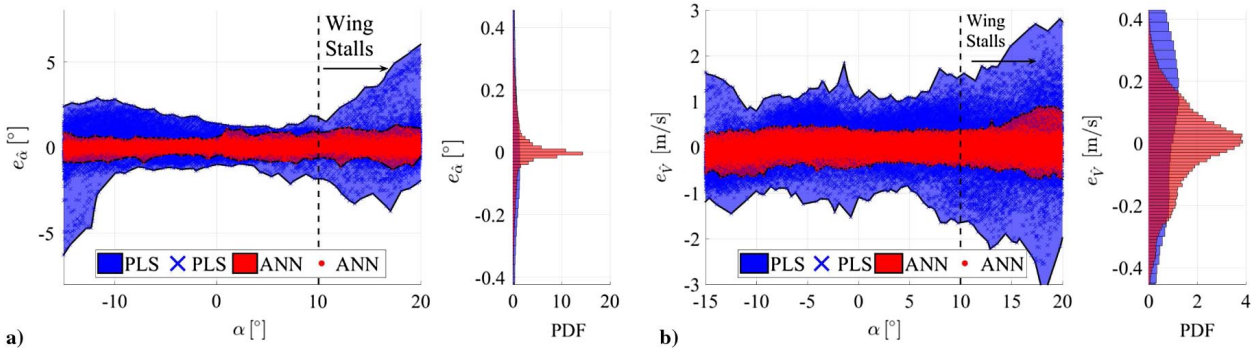

Fig. 12 Error distribution for estimation of aerodynamic variables using distributed sensing array: a) $e_{\hat{\alpha}}$ and b) $e_{\hat{V}}$.

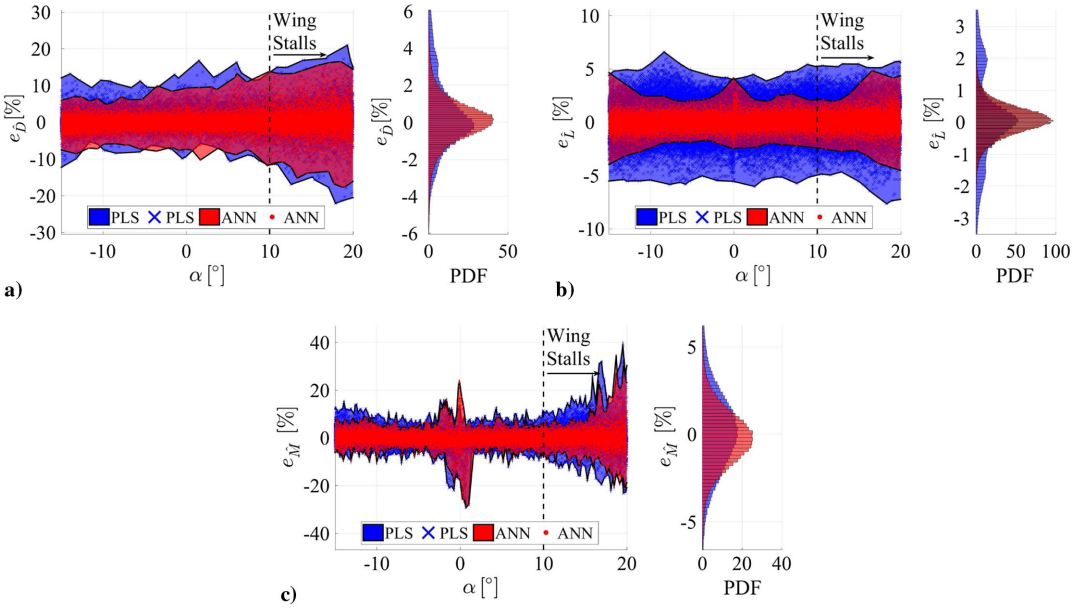

Fig. 13 Error distribution for estimation of aerodynamic loads using distributed sensing array: a) $e_{\hat{D}}$, b) $e_{\hat{L}}$, and c) $e_{\hat{M}}$.

slightly wider in the stall region ($\alpha \geq 10$ deg). The ANN-based estimator error distribution is better than the PLS-based estimator error distribution, with a RMSE of 0.64 N for the PLS-based estimator against 0.44 N for the ANN-based estimator. Measured L ranged from −33.39 to 49 N (i.e., measurement range of 82.39 N; Table 3). Note that the $e_{\hat{L}}$ distribution for the PLS estimator has three peaks: a central one on $e_{\hat{L}} = 0\%$ and two smaller ones (one at $e_{\hat{L}} \approx 2\%$ and another at $e_{\hat{L}} \approx -1.5\%$). This means that the PLS estimator tends to produce more scatter L estimates.

Figure 13c shows the $e_{\hat{M}}$ boundary across α and the distribution of $e_{\hat{M}}$. The ANN-based and PLS-based estimators error boundaries are very similar across α. The width of both boundaries significantly increases for $\alpha \geq 10$ deg. A decrease in performance is observed at $\alpha \approx 0$ deg. This is thought to be related to some outlier points from the torsional strain signal at $\alpha \approx 0$ deg (see Figs. 4e and 4f) because both estimators belong to the dynamic PVTS class (see Table 2) and make use of all available sensor signals. The error distribution for the ANN-based estimator and the PLS-based estimator are practically the same, with both RMSEs for the PLS-based estimator and the ANN-based estimator equal to 0.04 and 0.03 N m, respectively. For reference measured M ranged from −0.69 to 0.60 N · m (i.e., measurement range of 1.29 N · m; Table 3). The $e_{\hat{M}}$ PDF for the PLS estimator is not symmetric, with a slight tendency toward $e_{\hat{M}} > 0\%$. This means that PLS-based estimations of M tend to be underpredictions.

V. Discussion

In this paper, the signal characteristics of a distributed array of sensors measuring the loads (strain) and flow distribution (pressure) acting over the surface of an instrumented wind-tunnel wing model were measured. These signals were then used to build various nonlinear (ANN-based) and linear (PLS-based) predictors to estimate the aerodynamic variables and loads: α, V, D, L, and M.

Wind-tunnel characterization tests of pressure and strain signals showed that there was a wealth of information available in the pressure and strain signals. This included information on the attachment state of the flow and capturing nonlinear behaviors such as hysteresis and pitch rate dependent effects. These signals also showed strong correlation with parameters that cannot easily be measured in free flight, such as lift and drag forces. Here, it is shown that all these characteristics can then be estimated using the signals from the distributed array. These estimates of aerodynamic variables and loads could be used as inputs for flight control, supplying richer data than provided by conventional sensor suites.

In the characterization results, it was observed that q significantly changes the shape and magnitude of both the pressure and strain signals (Fig. 4). Based on this behavior and the available data, ANN-based estimators were organized using a three-level classification. It was observed that depending on the class, the performance of the ANN-based estimators improved in the following descending order of importance: 1) for training data, estimators with dynamic training data outperformed the matching estimators trained with quasi-static data; 2) for availability of inertial data q, the availability of inertial information improved performance; and 3) for distributed sensing data combination, in general, progressive improvement was observed as the amount of input data increased (PVTS/PVS is better than P, which in turn is better than VS/VTS).

It was observed that all ANN-based estimators only using combinations of vertical strain and vertical-torsional strain stood out as the worst performing in each estimator class. This is likely to be related in part to airspeed/dynamic pressure information not being explicitly fed into any of these estimators, making them particularly unsuitable for measuring aerodynamic variables. However, from characterization experiments, it was observed that the normalized vertical strain signals are highly correlated to the normal force (Fig. 4), behaving in a linear fashion for small α, which suggests that vertical strain could be used to estimate normal force rather than aerodynamic variables. Another reason for the reduced performance might be the highly nonlinear behavior of the torsional strain signal with α as well as the signal's poor signal-to-noise ratio.

The performance of the ANN-based estimators for the aerodynamic variables α and V was significantly better than that for the PLS-based estimators, suggesting that when using a distributed sensing array, a nonlinear estimator (ANN-based) might be better suited to estimate these aerodynamic variables. This is likely to be due to the aerodynamic variables being more highly correlated with the pressure sensor data than the strain data (Fig. 8) and the nonlinear nature of the ANN being more suited for the nonlinearity of the pressure signals (Fig. 4), especially at higher α.

The best-performing ANNs were able to accurately predict α and V even in the stall region, with overall validation RMSEs of 0.15 deg and 0.15 m/s (0.24 deg and 0.20 m/s for $\alpha > 10$ deg), respectively. Similar levels of accuracy have been obtained in wind-tunnel experiments with arrays of sensors mounted on wings in prestall conditions [17,18,27–30]. It was observed that the α estimator is able to deal with unsteady, nonlinear phenomena, removing hysteretic effects to provide an accurate estimate in high α at high dynamic rates. This suggests that ANN-based aerodynamic variable estimators that use pressure and strain data as input may be used to provide reliable α and V estimates at high α under dynamic conditions.

The level of estimation performance for loads was very similar for ANN-based and PLS-based estimators, suggesting that when using a

distributed sensing array, a linear estimator might be sufficient to estimate D, L, and M. Considering estimation of D, L, and M, the best-performing ANNs were able to achieve overall validation RMSEs of 0.35 N, 0.44 N, and 0.030 N · m, respectively; and the PLS achieved 0.54 N, 0.64 N and 0.036 N m. Both types of estimators also provided good estimates in the stall region. These values are of the same order of magnitude as other research using distributed sensing in wind-tunnel experiments [18]. It was observed that both the L estimators were able to accurately reconstruct hysteretic behavior. This suggests that load estimators that use pressure and strain data as input may be used to exploit dynamic behavior like dynamic lift to improve the maneuverability of UAVs.

Overall, the results presented here indicate that a linear estimator (PLS) is sufficient to estimate aerodynamic loads, whereas a nonlinear estimator (ANN) might be more appropriate to estimate aerodynamic variables. Additionally, these results suggest that pressure and strain sensing could be used in combination with nonlinear estimators to improve flight control performance by providing accurate estimates of aerodynamic variables and loads. The aerodynamic variables could be fed into model-based controllers, or the aerodynamic loads could be used directly by physics-based controllers [19,31,32]. Alternatively, a more robust estimate of the aircraft's dynamic state can be obtained by fusing the signals from the distributed array with the inertial and visual information of conventional sensors. It has been hypothesized that a similar approach known as "mode sensing" may be used by insects [8]. Another alternative is to use an end-to-end learning approach where systems, typically using convolutional neural networks, are trained to learn direct mappings between control inputs and system outputs [33], resulting in smaller networks with improved performance due to the internal component self-optimization.

To develop this approach further, there are a number of areas of potential development. A factor that has not been considered so far in the estimation algorithm is the signal response to control surface deflections. For the system to provide accurate estimates, a model of the signal response to control inputs needs to be included. One way of achieving this would be for an estimator to take into account the correlation between control inputs and the expected sensory response, and to then filter out the expected sensor response. This estimator would only then provide the signal generated by any external changes. It has been suggested that a similar adaptive filter approach is part of the function of the cerebellum in the mammalian nervous system [34], with other animal groups having equivalent systems involved with their motor control. A potential extension to the results presented could be to consider the case of highly flexible wings. Under this scenario, it is likely that a greater number of sensors distributed across the wing would be necessary to capture the full complexity of the wing dynamics. The position and number of sensors could then be optimized to maximize the observability of the parameters of interest. Future work could also focus on finding estimators that provide similar performance to ANNs but allow for physical interpretation of its structure and corresponding parameters. In particular, estimators using functional relationships between the measured signals and the quantities being estimated (e.g., Kalman filter, extended Kalman filter) should be considered.

VI. Conclusions

Wind-tunnel testing showed that a range of aerodynamic and load states can be estimated using the signals from a distributed array of pressure and strain sensors on a wing. The use of the distributed array allowed accurate estimates to be made even when the flow became unsteady and captured nonlinear behaviors such as stall, hysteresis, and pitch rate dependent effects. It was found that nonlinear ANN estimators were robust and gave good estimates of aerodynamic variables and loads, whereas linear PLS estimators performed well when estimating loads but were less accurate at estimating aerodynamic variables.

Overall, these results indicate that bioinspired sensors, sensory processing, and potentially neural inspired control structures offer an alternative way to thinking about aircraft flight control. Future applications based on distributed sensing could include enhanced flight control systems that directly use measurements of aerodynamic states and loads, allowing for increase maneuverability and improved control. This could be particularly useful for unmanned aerial vehicles with high degrees of freedom such as highly flexible or morphing wings, where the airflow and loads vary dynamically across the wing, depending on the configuration of the wing as well as the current aerodynamic conditions.

Acknowledgments

This project has received funding from the European Research Council under the European Union's Horizon 2020 Research and Innovation Programme (grant agreement no. 679355). The authors would like to thank Lee Winter from the University of Bristol Wind Tunnel Laboratory for his invaluable support and work during the assembly of the pressure ports in the pressure sensing platform that was used to carry out the experiments presented in this paper.

References

[1] Mohamed, A., Clothier, R., Watkins, S., Sabatini, R., and Abdulrahim, M., "Fixed-Wing MAV Attitude Stability in Atmospheric Turbulence Part 1: Suitability of Conventional Sensors," *Progress in Aerospace Sciences*, Vol. 70, Oct. 2014, pp. 69–82. https://doi.org/10.1016/j.paerosci.2014.06.001

[2] Taylor, G. K., Carruthers, A. C., Hubel, T. Y., and Walker, S. M., "Wing Morphing in Insects, Birds and Bats: Mechanism and Function," *Morphing Aerospace Vehicles and Structures*, edited by J. Valasek, Wiley, New York, 2012, pp. 11–40. https://doi.org/10.1002/9781119964032.ch2

[3] Watkins, S., Milbank, J., Loxton, B. J., and Melbourne, W. H., "Atmospheric Winds and Their Implications for Microair Vehicles," *AIAA Journal*, Vol. 44, No. 11, 2006, pp. 2591–2600. https://doi.org/10.2514/1.22670

[4] Young, J., Walker, S. M., Bomphrey, R. J., Taylor, G. K., and Thomas, A. L., "Details of Insect Wing Design and Deformation Enhance Aerodynamic Function and Flight Efficiency," *Science*, Vol. 325, No. 5947, 2009, pp. 1549–1552. https://doi.org/10.1126/science.1175928

[5] Muijres, F., Johansson, L. C., Barfield, R., Wolf, M., Spedding, G., and Hedenström, A., "Leading-Edge Vortex Improves Lift in Slow-Flying Bats," *Science*, Vol. 319, No. 5867, 2008, pp. 1250–1253. https://doi.org/10.1126/science.1153019

[6] Shepard, E. L., Williamson, C., and Windsor, S. P., "Fine-Scale Flight Strategies of Gulls in Urban Airflows Indicate Risk and Reward in City Living," *Philosophical Transactions of the Royal Society of London, Series B: Biological Sciences*, Vol. 371, No. 1704, 2016, Paper 20150394. https://doi.org/10.1098/rstb.2015.0394

[7] Mallon, J. M., Bildstein, K. L., and Katzner, T. E., "In-Flight Turbulence Benefits Soaring Birds," *Auk: Ornithological Advances*, Vol. 133, No. 1, 2015, pp. 79–85. https://doi.org/10.1642/AUK-15-114.1

[8] Taylor, G. K., and Krapp, H. G., "Sensory Systems and Flight Stability: What Do Insects Measure and Why?" *Insect Mechanics and Control, Advances in Insect Physiology*, edited by J. Casas, and S. Simpson, Vol. 34, Academic Press, London, 2007, pp. 231–316. https://doi.org/10.1016/S0065-2806(07)34005-8

[9] Hörster, W., "Histological and Electrophysiological Investigations on the Vibration-Sensitive Receptors (Herbst Corpuscles) in the Wing of the Pigeon (Columba Livia)," *Journal of Comparative Physiology A*, Vol. 166, No. 5, 1990, pp. 663–673. https://doi.org/10.1007/BF00240016

[10] Brown, R. E., and Fedde, M. R., "Airflow Sensors in the Avian Wing," *Journal of Experimental Biology*, Vol. 179, No. 1, 1993, pp. 13–30.

[11] Altshuler, D. L., Bahlman, J. W., Dakin, R., Gaede, A. H., Goller, B., Lentink, D., Segre, P. S., and Skandalis, D. A., "The Biophysics of Bird Flight: Functional Relationships Integrate Aerodynamics, Morphology, Kinematics, Muscles, and Sensors 1," *Canadian Journal of Zoology*, Vol. 93, No. 12, 2015, pp. 961–975. https://doi.org/10.1139/cjz-2015-0103

[12] Sterbing-D'Angelo, S., Chadha, M., Chiu, C., Falk, B., Xian, W., Barcelo, J., Zook, J. M., and Moss, C. F., "Bat Wing Sensors Support Flight Control," *Proceedings of the National Academy of Sciences*, Vol. 108, No. 27, 2011, pp. 11291–11296. https://doi.org/10.1073/pnas.1018740108

[13] Whitmore, S., Cobleigh, B., and Haering, E., Jr., "Design and Calibration of the X-33 Flush Airdata Sensing (FADS) System," *36th AIAA Aero-*

space Sciences Meeting and Exhibit, AIAA Paper 1998-0201, 1998. https://doi.org/10.2514/6.1998-201

[14] Pruett, C., Wolf, H., Heck, M., and Siemers, P., III, "Innovative Air Data System for the Space Shuttle Orbiter," *Journal of Spacecraft and Rockets*, Vol. 20, No. 1, 1983, pp. 61–69. https://doi.org/10.2514/3.28357

[15] Mark, A., Xu, Y., and Dickinson, B. T., "Review of Microscale Flow-Sensor-Enabled Mechanosensing in Small Unmanned Aerial Vehicles," *Journal of Aircraft*, Vol. 56, No. 3, 2019, pp. 962–973. https://doi.org/10.2514/1.C034979

[16] Shen, H., Xu, Y., and Remeikas, C., "Pitch Control of a Micro Air Vehicle with Micropressure Sensors," *Journal of Aircraft*, Vol. 50, No. 1, 2013, pp. 239–248. https://doi.org/10.2514/1.C031894

[17] Fei, H., Zhu, R., Zhou, Z., and Wang, J., "Aircraft Flight Parameter Detection Based on a Neural Network Using Multiple Hot-Film Flow Speed Sensors," *Smart Materials and Structures*, Vol. 16, No. 4, 2007, Paper 1239. https://doi.org/10.1088/0964-1726/16/4/035

[18] Magar, K. T., Reich, G. W., Kondash, C., Slinker, K., Pankonien, A. M., Baur, J. W., and Smyers, B., "Aerodynamic Parameters from Distributed Heterogeneous CNT Hair Sensors with a Feedforward Neural Network," *Bioinspiration and Biomimetics*, Vol. 11, No. 6, 2016, Paper 066006. https://doi.org/10.1088/1748-3190/11/6/066006

[19] Yeo, D., Atkins, E. M., Bernal, L. P., and Shyy, W., "Experimental Validation of an Aerodynamic Sensing Scheme for Post-Stall Aerodynamic Moment Characterization," *AIAA Atmospheric Flight Mechanics (AFM) Conference*, AIAA Paper 2013-4979, 2013. https://doi.org/10.2514/6.2013-4979

[20] Wood, K. T., Araujo-Estrada, S., Richardson, T., and Windsor, S., "Distributed Pressure Sensing-Based Flight Control for Small Fixed-Wing Unmanned Aerial Systems," *Journal of Aircraft*, Vol. 56, No. 5, 2019, pp. 1–10. https://doi.org/10.2514/1.C035416

[21] Thompson, R. A., Evers, J., and Stewart, K., "Attitude Control Augmentation Using Wing Load Sensing-A Biologically Motivated Strategy," *Atmospheric Flight Mechanics Conference*, AIAA Paper 2010-7936, 2010. https://doi.org/10.2514/6.2010-7936

[22] Castano, L., Airoldi, S., McKenna, T., and Humbert, J. S., "Gust Rejection Using Force Adaptive Feedback for Roll," *14th AIAA Aviation Technology, Integration, and Operations Conference*, AIAA Paper 2014-2588, 2014. https://doi.org/10.2514/6.2014-2588

[23] Araujo-Estrada, S. A., Salama, F., Greatwood, C. M., Wood, K. T., Richardson, T. S., and Windsor, S. P., "Bio-Inspired Distributed Strain and Airflow Sensing for Small Unmanned Air Vehicle Flight Control," *AIAA Guidance, Navigation, and Control Conference*, AIAA Paper 2017-1487, 2017. https://doi.org/10.2514/6.2017-1487

[24] Barrett, R., "Design and Performance of a New Low Turbulence Wind Tunnel at Bristol University," *Aeronautical Journal*, Vol. 88, No. 873, 1984, pp. 86–90. https://doi.org/10.1017/S000192400002025X

[25] Hornik, K., Stinchcombe, M., and White, H., "Multilayer Feedforward Networks Are Universal Approximators," *Neural Networks*, Vol. 2, No. 5, 1989, pp. 359–366. https://doi.org/10.1016/0893-6080(89)90020-8

[26] Rosipal, R., and Krämer, N., "Overview and Recent Advances in Partial Least Squares," *International Statistical and Optimization Perspectives Workshop "Subspace, Latent Structure and Feature Selection"*, Springer, Berlin, 2005, pp. 34–51. https://doi.org/10.1007/11752790_2

[27] Callegari, S., Zagnoni, M., Golfarelli, A., Tartagni, M., Talamelli, A., Proli, P., and Rossetti, A., "Experiments on an Aircraft Flight Parameter Detection by On-Skin Sensors," *Sensors and Actuators A: Physical*, Vols. 130–131, Aug. 2006, pp. 155–165. https://doi.org/10.1016/j.sna.2005.12.026

[28] Laurence, R. J., Argrow, B. M., and Frew, E. W., "Wind Tunnel Results for a Distributed Flush Airdata System," *Journal of Atmospheric and Oceanic Technology*, Vol. 34, No. 7, 2017, pp. 1519–1528. https://doi.org/10.1175/JTECH-D-16-0242.1

[29] Samy, I., Postlethwaite, I., Gu, D.-W., and Green, J., "Neural-Network-Based Flush Air Data Sensing System Demonstrated on a Mini Air Vehicle," *Journal of Aircraft*, Vol. 47, No. 1, 2010, pp. 18–31. https://doi.org/10.2514/1.44157

[30] Que, R., and Zhu, R., "Aircraft Aerodynamic Parameter Detection Using Micro Hot-Film Flow Sensor Array and BP Neural Network Identification," *Sensors (Switzerland)*, Vol. 12, No. 8, 2012, pp. 10,920–10,929. https://doi.org/10.3390/s120810920

[31] Shen, H., Xu, Y., and Dickinson, B. T., "Micro Air Vehicle's Attitude Control Using Real-Time Pressure and Shear Information," *Journal of Aircraft*, Vol. 51, No. 2, 2014, pp. 661–671. https://doi.org/10.2514/1.C032375

[32] Marino, M. J., Watkins, S., Sabatini, R., and Gardi, A., "Sensing Unsteady Pressure on MAV Wings: A New Method for Turbulence Alleviation," *Applied Mechanics and Materials*, Vol. 629, Oct. 2014, pp. 48–54. https://doi.org/10.4028/www.scientific.net/AMM.629.48

[33] Bojarski, M., Testa, D. D., Dworakowski, D., Firner, B., Flepp, B., Goyal, P., Jackel, L. D., Monfort, M., Muller, U., Zhang, J., Zhang, X., Zhao, J., and Zieba, K., "End to End Learning for Self-Driving Cars," Preprint, submitted 25 April 2016, https://arxiv.org/abs/1604.07316.

[34] Dean, P., Porrill, J., Ekerot, C.-F., and Jorntell, H., "The Cerebellar Microcircuit as an Adaptive Filter: Experimental and Computational Evidence," *Nature Reviews Neuroscience*, Vol. 11, No. 1, 2010, pp. 30–43. https://doi.org/10.1038/nrn2756